# UV Photodesorption and photoconversion of interstellar ices: the laboratory perspective

Bulak, M.

# 5 | UV PHOTODESORPTION AND PHOTOCONVERSION RATES OF $H_2O$ ICE - MEASURED WITH LASER DESORPTION POST IONIZATION MASS SPECTROMETRY


## Abstract

Ultraviolet (UV) photodesorption of water ($H_2O$) ice is a non-thermal desorption mechanism required to account for detected abundances of gas-phase water ($H_2O$) towards cold regions within the interstellar medium (ISM). Previous experimental and theoretical studies provide a range of photodesorption rates for $H_2O$ ice, and point to a convoluted competition between molecular processes following an absorption of a UV photon in the ice. A quantitative measurement allowing for separation of the effect of photodesorption and photoconversion during the photolysis of $H_2O$ ice is still lacking. Here we aim to quantify the effects of photodesorption and photoconversion upon UV photolysis of a $H_2O$ ice. A porous amorphous $H_2O$ ice at 20 K is processed with UV photolysis (photon energy of 7-10.2 eV) and compared to an identical experiment with an additional layer of argon coating. To trace the ice composition and thickness, laser desorption post ionization time-of-flight mass spectrometry (LDPI TOF MS) is utilized. A comparison between (un)coated experiments allows to derive information about the photoconversion and photodesorption of the ice and quantify the latter. We derive the total photodesorption rate for a porous amorphous $H_2O$ ice at 20 K to be $(1.0 \pm 0.2) \times 10^{-3}$ per incident UV photon (7 – 10.2 eV), in agreement with the available literature. Based on this value, we place an upper limit on the intact ($H_2O$) and dissociative (OH) desorption rates, equal to $1.0 \times 10^{-3}$ per incident UV photon, while for reactive desorption ($O_2$), this limit is equal to $0.5 \times 10^{-3}$ per incident UV photon. Photoconversion depletes the $H_2O$ ice at a rate of $(2.3 \pm 0.2) \times 10^{-3}$ per incident UV photon.



Bulak, M., Paardekooper, D.M., Fedoseev, G., Samarth, P., Linnartz, H., to be submitted

## 5.1 Introduction

Water ($H_2O$) is ubiquitous in the interstellar medium (ISM) and plays a key role in the physics and chemistry of the star- and planet-forming regions. It is the most abundant constituent of the interstellar ice mantles (Gibb et al. 2004; Boogert et al. 2008), and has an observed gas-phase trail in different environments, including diffuse and translucent clouds (Flagey et al. 2013), prestellar cores (Caselli et al. 2012), star-forming regions (Ceccarelli et al. 2010), protoplanetary disks (Hogerheijde et al. 2011), and comets (Hartogh et al. 2011). The observed abundances of water in the ice and gas are intricately linked, and provide information on local physical conditions.

The majority of water in the ISM resides in interstellar ices with an average abundance of solid $H_2O$ with respect to gas-phase $H_2$ equal to $1.0 \times 10^{-4}$ (e.g., Pontoppidan et al. 2004; Boogert et al. 2015; Whittet et al. 2013). Water ice is mainly formed on cold dust grains (10 – 20 K) via surface hydrogenation reactions with O, OH, $O_2$, and $O_3$ (Tielens & Hagen 1982; Bergin et al. 2000; Ioppolo et al. 2008, 2010; Miyauchi et al. 2008; Lamberts et al. 2013). An additional low-temperature formation channel is available via gas-phase chemistry. This contribution is limited by the efficiency of the involved ion-molecule reaction scheme, and is capable of reproducing the water abundances of $H_2O/H_2$ only at the level of $(0.5 - 1.5) \times 10^{-8}$, equivalent to abundances found in translucent clouds (Bergin et al. 1995; Jensen et al. 2000; Hollenbach et al. 2009). An alternative gas-phase formation pathway via neutral-neutral chemistry becomes efficient only above temperatures of 250 K (Harada et al. 2010).

The ice chemistry is coupled with processes in the gas-phase via accretion and desorption processes. In regions with temperatures between 10 – 20 K, observed gas-phase water abundances cannot be accounted for by gas-phase formation or thermal desorption, hence non-thermal desorption mechanisms need to be considered (Willacy & Langer 2000; Boonman et al. 2003; Öberg et al. 2009d; Hollenbach et al. 2009; Walsh et al. 2010; Oka et al. 2012). This has been the case for observations towards photon dominated regions of molecular clouds (Snell et al. 2000; Wilson et al. 2003), prestellar cores (Caselli et al. 2012), outer parts of protostellar envelopes (Schmalzl et al. 2014) and protoplanetary disks (Dominik et al. 2005; Willacy 2007; Hogerheijde et al. 2011). The non-thermal desorption mechanism that is used to explain these observations is UV photodesorption of water ice. This mechanism, initiated by a UV photon absorption (6 – 13.6 eV), allows species in the ice to be transferred into the gas-phase. For this process to take place, UV photons are required, which originate from the interstellar radiation field (ISRF) and nearby protostars. In regions where ISRF is attenuated by dust grains (i.e., cores of dense clouds or protoplanetary disks), the (lower) photon flux originates from interactions of cosmic rays with $H_2$, resulting in a secondary UV field, with emission peaking at Ly-$\alpha$ (Prasad & Tarafdar 1983; Gredel et al. 1989). For these reasons photodesorption of interstellar ice analogues has been studied in detail, both experimentally and theoretically for a number of different molecules, including CO, $CO_2$, $CH_4$, $CH_3OH$, and also $H_2O$.

An experimental determination of the photodesorption rate is inherently challenging due to the convoluted competition between photodesorption and photoconversion in UV-irradiated interstellar ices (see Fig. 1 in Bulak et al. 2020). Photoconversion is characterized by a combination of the following two solid state processes: photodissociation, followed by recombination reactions into photoproducts (defined as photochemistry), and reactions of nondissociated, photoexcited molecules, with neighboring

neutral species. Both types of reactions provide formation pathways of many of the observed simple and complex species (e.g., Gerakines et al. 1996; Garrod et al. 2008; Öberg et al. 2009c; Paardekooper et al. 2016b; Bulak et al. 2021). The competition between photodesorption and photoconversion usually takes place for species with a bond dissociation energy below the energy of impacting UV photons, which applies to most constituents of interstellar ices found in the dense molecular clouds, $H_2O$, $CO_2$, $CH_4$, $NH_3$, $CH_3OH$. The common exceptions are CO and $N_2$, which have a bond dissociation energy above 10.2 eV.

The photodesorption and photoconversion of $H_2O$ ice have been extensively studied experimentally (Westley et al. 1995a; Gerakines et al. 1996; Öberg et al. 2009d; DeSimone et al. 2013; Cruz-Diaz et al. 2018), and with molecular dynamics simulations (Andersson et al. 2006; Andersson & van Dishoeck 2008; Arasa et al. 2010, 2011, 2015; Koning et al. 2013). In the original laboratory studies, a quartz micro-balance was used to monitor the depletion of $H_2O$ ice upon UV irradiation and used to derive the photodesorption rate. Simultaneously, photodesorbed gas phase species, $H_2$ and $O_2$, were monitored by quadrupole mass spectrometry (QMS). In a study focusing on the photoconversion of $H_2O$ ice, Gerakines et al. (1996) used infrared spectroscopy (IR) to detect the formation of $HO_2$, $H_2O_2$, and OH in the ice. In the work by Öberg et al. (2009d), the photodepletion upon UV radiation (7 – 10.2 eV) of the $H_2O$ and $D_2O$ ices was monitored using reflection-absorption infrared spectroscopy (RAIRS) while the gas-phase species were probed by a QMS. Based on the collected RAIRS data, the photodesorption rate of $H_2O$ ice was derived. Mass spectrometry measurements allowed to detect photodesorption of OH, a gas-phase product of solid water photodissociation, as well as other photoproducts ($H_2$, $O_2$). In more recent studies (Cruz-Diaz et al. 2018; Fillion et al. 2021), a QMS was used to measure the gas-phase signal during the photolysis of $H_2O$ ($D_2O$) ice. Based on the calibration of the QMS, the signal was converted to a photodesorption rate of $H_2O$, OH and $O_2$. In the work of Fillion et al. (2021) a wavelength selective (and not a broad band) approach was used, as originally introduced by Fayolle et al. (2011).

The aforementioned diagnostic tools, IR spectroscopy and QMS, have been proven capable tools to quantify the photon - triggered processes, providing a range of photodesorption rates for $H_2O$ ice at different low temperatures between $(1 - 4) \times 10^{-3}$ mol. photon$^{-1}$. However, a method capable of simultaneously characterizing the effect of photodesorption and photoconversion in water ice is still missing. IR spectroscopy allows to trace photodepletion of the parent species, which is a combined effect of both processes. It is a method which requires molecules to have an IR-active transition, which means that a-polar species, such as one of the photoproducts, $O_2$, are simply invisible. In addition, there is an uncertainty associated with the interpretation of the IR data, linked to a possible overlap of vibrational features of the parent species ($H_2O$) with photoproducts (OH) and the mathematical deconvolution of the photodesorption rate. Mass spectrometry (QMS) offers a solution to these issues with a direct measurement of photodesorbed species, however, it also comes with limitations. QMS measures an equilibrated gas-phase composition in the chamber, which means that molecules, prior to being detected, may interact with the walls and other inner parts of the setup. In addition, the conversion of the gas-phase signals to a photodesorption rate is challenging (Fayolle et al. 2011; Martín-Doménech et al. 2015b; Bertin et al. 2016); also, with a QMS-only approach, the effect of photoconversion in the ice remains unconstrained.

In this study of UV photolysis of amorphous water ice, we apply a different experimental approach, which has been previously used to measure the photodesorption of CO (Paardekooper et al. 2016c) and that was shown to separate photodesorption effects from photoconversion in pure ices of $CH_4$, $CH_3OH$, and $CH_3CN$ (Bulak et al. 2020). To determine the effect of each process, pure $H_2O$ ice photolysis experiments are compared to measurements with an additional argon coating. The role of the argon layer is to quench any type of photon-triggered desorption, with a minimal effect on the photoconversion. Laser desorption post ionization time of flight mass spectrometry (LDPI TOF MS) is used to probe the ice composition and thickness as a function of UV fluence. The comparison of (un)coated experiments is used to trace both processes, photoconversion and photodesorption, and to quantify the latter. This offers a fully independent method to derive the photodesorption rate of $H_2O$ ice. The next section includes a summary of the experimental procedure, while the results, discussion and astrophysical implications are described in sections 5.3, and 5.4, and 5.5, respectively.

## 5.2 Experimental

A detailed description of MATRI$^2$CES (Mass Analysis Tool to study Reactions in Interstellar ICES) is provided in Paardekooper et al. 2014. The experimental procedure that has been used is described in Bulak et al. 2020. In this section we only briefly discuss the relevant details.

### 5.2.1 Experimental system

MATRI$^2$CES consists of a main and time of flight mass spectrometer (TOF MS) chamber with a base pressure in the $\sim 10^{-10}$ mbar range. In the main chamber, ices are deposited onto a chemically inert gold surface, cooled with a closed cycle helium cryostat to 20 K. The cryostat is mounted on a two dimensional translation stage which allows to manipulate the position of substrate along the horizontal and vertical axis. The temperature of the substrate is regulated in the 20 - 300 K range (relative precision of $\pm$ 0.25 K) using a thermocouple and a resistive heater in thermal contact with the substrate, controlled by a Lakeshore temperature controller. Prior to deposition, liquid water samples of $H_2{}^{16}O$ (miliQ) or $H_2{}^{18}O$ (Sigma-Aldrich, 97%$^{18}$O) are purified from air contamination via three freeze-pump-thaw cycles. Argon gas ($\geq$ 99,999 % purity, Linde) is used without further purification. The deposition of ($H_2O$ and Ar) vapors proceeds through a capillary pointed at 85 degrees with respect to the substrate. The ice growth rate is controlled via a calibrated high precision needle valve. As a result of deposition at 20 K, we form a thin film of porous amorphous solid water (ASW) with an ice column density of $20 \times 10^{15}$ molecules cm$^{-2}$ (20 monolayers, ML, assuming 1 ML = $1 \times 10^{15}$ molecules cm$^{-2}$ ). The uniformity of the ice thickness across the substrate is $\pm$ 1.5 ML. The thickness of the deposited argon coating is 50 ML, sufficient to prevent any forms of photodesorption of the underlaying ice (see Bulak et al. 2020).

The photolysis is performed with a microwave discharge hydrogen lamp (MDHL), which emits UV photons in the range between 121.6 - 170 nm. This corresponds to an energy range of 7.2 – 10.2 eV. The spectral energy distribution (SED) of the lamp

is given in Ligterink et al. 2015 (see Fig. 4 therein) and the UV photon flux was calibrated at the location of the substrate using a Si diode to be (2.5 ± 0.5) × $10^{14}$ photons $cm^{-2}$ $s^{-1}$.

A laser desorption post ionization time of flight mass spectrometry (LDPI TOF MS) is used to quantitatively probe the composition of the ice. An unfocused laser shot (Nd:YAG, Polaris II, 4-5 ns) trimmed to a beam diameter of ∼1.5 mm with a typical pulse energy of ∼ 55 mJ per $cm^2$, is guided onto the deposited ice at an incident angle of 30 degrees with respect to the plane perpendicular to the substrate. This pulse, optimized to trigger a complete local desorption, transfers the species from the ice into the gas phase. The resulting plume is subsequently ionized via a continuous electron impact ionization source with a mean electron energy of 70 eV. As the ionized plume travels through the ion optics, a part of it is extracted with a short voltage pulse (typical duration of 4 $\mu$s), which guides the charged species into the field free TOF MS (operated in reflectron mode). During the drift, ions are separated based on their mass to charge ratio (m/z). Their time of flight, from the ion extraction area to the Z-gap micro channel plate detector (MCP), is recorded with a data acquisition card (DAQ) at a sampling rate of 2.5× $10^8$ Hz. This probing technique is synced with an automated translation of the substrate along the vertical direction which allows to probe 100 fresh locations on the substrate (along z-axis). To track changes in the ice as a function of UV photon fluence, the substrate is translated along the x-axis, the probing scheme is repeated for each UV dose along a fresh column of the ice. The TOF traces are collected and averaged using a Labview routine.

The probing sequence of the laser shot, the ion extraction pulse and the data acquisition is controlled with a delay generator (DG 535, Stanford Research System). A variation in a relative time delay between the laser shot and the ion extraction pulse (between 17 and 80 $\mu$s) allows to sample the complete profile of the plume. The collected TOF traces are subsequently converted to mass spectra, with a mass resolution of $\Delta m/m \sim 250$.

The LDPI TOF MS signature of $H_2O$ ice consists of mass peaks at m/z = 16, 17, and 18, which are fragments formed upon the electron impact ionization event: $O^+$, $OH^+$ and $H_2O^+$, accordingly (Kim et al. 2014). Due to the low relative intensity of the mass peak at m/z = 16 (1% of m/z = 18), only peaks at m/z = 17 and 18 are used for quantified analysis. For control experiments with $H_2{}^{18}O$, peaks at m/z = 19, and 20 are used.

The sum of the calculated intensities of $H_2O$ features in the plume profile is proportional to the thickness of the ice (Paardekooper et al. 2014; Bulak et al. 2020). To demonstrate this, $H_2O$ ices of different initial thickness (10 - 60 ML) were deposited and analyzed with LDPI TOF MS. In Figure 5.1, the total intensity of the recorded plume profile is shown as a function of the deposited ice thickness. The plot includes data from two separate calibration experiments, which probe ices with different initial ice thickness. The demonstrated linear relationship allows to use the integrated plume profile obtained with LDPI TOF MS as a direct measurement of the ice thickness.

### 5.2.2 Experimental overview

The UV photolysis experiments are aimed to separate the effect of photoconversion from photodesorption in a porous amorphous water ice. Following the approach of Bulak et al. 2020, the first type of experiment probes the photodepletion of pure $H_2O$

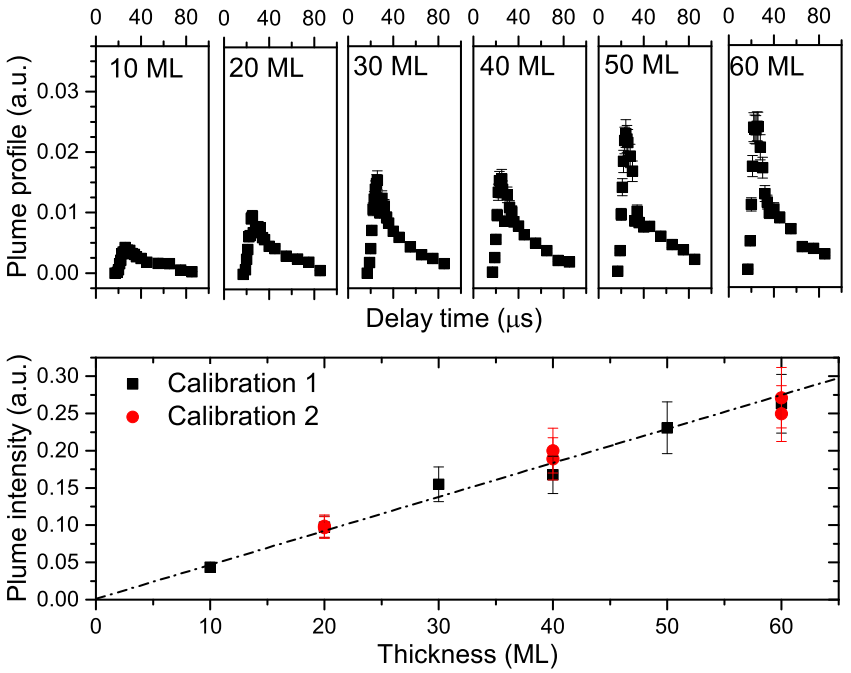


**Figure 5.1:** *Top panel:* LDPI TOF MS plume profiles for different initial $H_2O$ ice thickness at 20 K. Profiles are collected as a function of the delay time between laser desorption and ion extraction. *Bottom panel:* Total signal of the integrated plume profiles (top panel) as a function of initial ice thickness of amorphous $H_2O$ ice, collected during two independent calibration measurements. Data is fitted with a linear function ($R^2 = 0.98$).

ice. The measured loss of $H_2O$ is linked to the photodissociation (photoexcitation) of the parent species followed by formation of photoproducts (photoconversion) as well as photodesorption of the water molecules, its fragments and the photoproducts. The second type of experiment is performed with an additional layer of argon (50 ML) deposited on top of the $H_2O$ ice. The role of the coating is to quench photodesorption processes, including intact, dissociative, and reactive photodesorption (being surface or subsurface processes). Argon, as a noble gas, does not interact with the photodissociation products of $H_2O$. In addition, the argon coating is transparent in the UV range (Schnepp & Dressler 1960), allowing for a direct comparison of the two experiments. The difference in the photodepletion of $H_2O$ between (un)coated experiments is used to derive a total photodesorption rate in the $H_2O$ ice.

A challenge associated with measuring the photodesorption of water ice, is to exclude the contribution from the residual gas phase water, present in the vacuum chamber even at UHV conditions. The $H_2O$ freeze out is most efficient immediately after the ice deposition, and it continues during the UV photolysis (see Westley et al. 1995a and Öberg et al. 2009d), which is also the case in our system. The issue is circumvented by considering the relative difference in the photodepletion rate between (un)coated experiments, both of which include the contribution from the residual gas freeze out. Hence, the contamination is present, however, its impact on the derived

photodesorption rate is limited. The same reasoning is applied to the uncertainty related to other experimental parameters: UV photon flux and ice thickness calibration. Under the assumption that the argon layer has a minimum effect on the photon flux reaching the $H_2O$ ice, these main sources of uncertainty (photon flux and ice thickness), during the derivation of the photodesorption yield, cancel each other out. Hence, the error margin in this work is based on the reproducibility of the repeated measurements (15% for both coated, and uncoated experiments), which leads to a final uncertainty of 21% on the photodesorption yield.

The experimental parameters were constrained in the following way. The initial ice thickness is set within the characterized linear range (see Fig. 5.1), that is above the threshold (4 - 5 ML), at which the photodesorption is no longer expected to be a zeroth order process (Öberg et al. 2009d; Muñoz Caro et al. 2010; Fayolle et al. 2011; Chen et al. 2014). The substrate temperature during the deposition and irradiation is kept at 20 K, the minimum reachable temperature, aiming to represent the "warm" regions of dense molecular clouds. To be able to monitor the photodepletion of $H_2O$ abundance, the ices are exposed to a UV photon fluence (in increments) amounting to $4.5 \times 10^{18}$ photons cm$^{-2}$. The experiments with the argon coating are also performed at 20 K, which is well below the sublimation threshold of argon between 30 and 40 K.

## 5.3 Results

Figure 5.2A. shows the LDPI TOF MS spectra of $H_2O$ ice at 20 K prior to UV irradiation. The recorded plume profile, based on the peaks characteristic for water ($OH^+$ and $H_2O^+$), is used as a reference spectrum to track changes in the ice as a function of UV photon fluence. The observed multiple traces of water ions are representative of different parts of the plume, each collected at a separate extraction time (see Section 5.2.1). To demonstrate the evolution of the $H_2O$ ice upon UV irradiation, Figure 5.2B. shows the LDPI TOF MS plume profile recorded after a UV dose of $2.7 \times 10^{18}$ photons cm$^{-2}$. The plume (without argon coating) shows the same distribution profile, with a clear decrease in the intensity of the ion signals, which is linked to the photodepletion of the $H_2O$ ice.

To derive the photodepletion rate, LDPI TOF MS plume profiles have been recorded at six increments of UV photon fluence, with the final fluence equal to $4.5 \times 10^{18}$ photons cm$^{-2}$. Figure 5.2C. shows the corresponding integrated LDPI TOF MS spectra, which are converted to the ice column density, following the methods described in Section 5.2. The resulting column density (for experiments with both $H_2{}^{16}O$ and $H_2{}^{18}O$) are plotted in Fig. 5.2D. The best fit to the data is provided by a linear function ($R^2 = 0.989$), where the slope represents the photodepletion rate of $H_2O$ ice at 20 K. The calculated value is equal to $(3.4 \pm 0.1) \times 10^{-3}$ molecule photon$^{-1}$. It accounts for losses of amorphous $H_2O$ ice due to photoconversion and photodesorption events. After the maximum photon fluence of $4.5 \times 10^{18}$ photons cm$^{-2}$, 75% of the $H_2O$ ice is depleted, yielding a final column density of $(5.1 \pm 1.5) \times 10^{15}$ molecules cm$^{-2}$.

A similar analysis has been performed on the LDPI TOF MS spectra of $H_2O$ ice capped with an argon layer (50 ML) at 20 K, shown in Figure 5.3(A-D). In the mass spectra prior to UV irradiation, in addition to the features assigned to $H_2O$, signal representing $Ar^+$ is traced (Fig. 5.3A). To demonstrate the decrease of the $H_2O$ ice upon UV irradiation, the plume profile after a fluence of $3.6 \times 10^{18}$ photons cm$^{-2}$ is

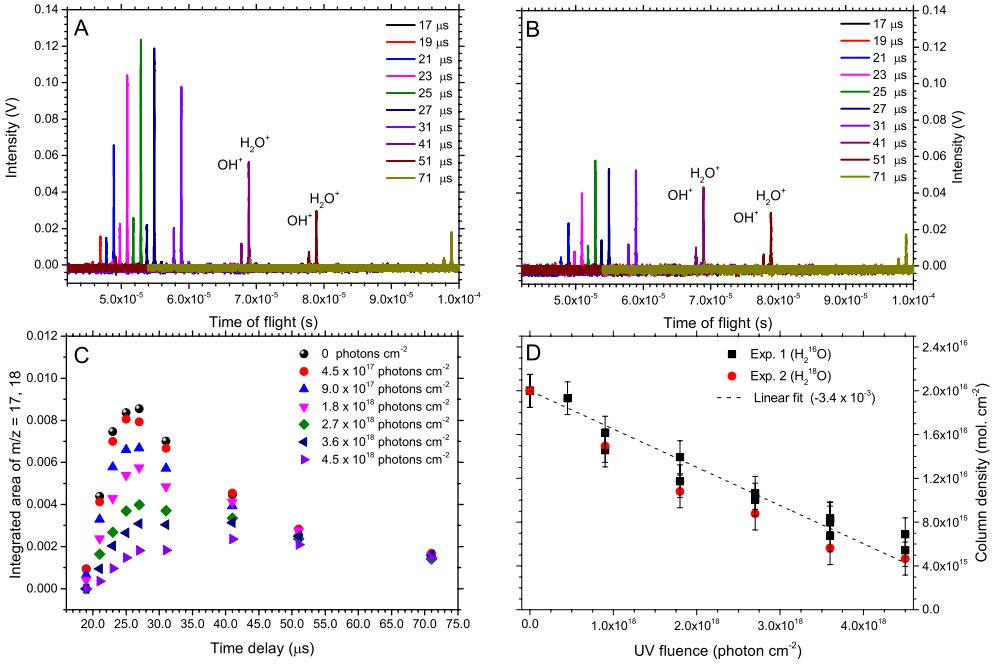


**Figure 5.2:** *Panel A:*LDPI TOF MS spectra of porous amorphous $H_2O$ ice (20 ML) collected at 20 K, prior to UV photolysis. *Panel B:* LDPI TOF MS spectra of porous amorphous $H_2O$ ice after an UV irradiation with a photon fluence of 2.7 $\times$ $10^{18}$ photons $cm^{-2}$. *Panel C:* Integrated plume profiles of LDPI TOF MS signals for different UV photon fluence increments. *Panel D:* Photodepletion of the $H_2O$ column density as a function of UV fluence from repeated experiments with $H_2{}^{16}O$ and $H_2{}^{18}O$. Error bars represent the uncertainty on the ice thickness of $\pm$1.5 ML.

shown (Fig. 5.3B). The integrated mass peaks for all UV fluence increments are then converted into the corresponding ice column density (Fig. 5.3C and 5.3D). The data from two experiments (water with $^{16}O$ and $^{18}O$) is fitted with a linear function with the slope equal to (2.3 $\pm$ 0.3) $\times$ $10^{-3}$ molecule $photon^{-1}$ ($R^2$ = 0.99). In the experiment with argon coating, the loss of $H_2O$ via photodesorption channels is quenched, while the loss channel due to photoconversion remains active. After the maximum photon fluence of 4.5 $\times$ $10^{18}$ photons $cm^{-2}$, $\sim$55% of the $H_2O$ ice is depleted, resulting in a column density of (9.2 $\pm$ 1.5) $\times$ $10^{15}$ molecules $cm^{-2}$. Due to the timing optimized for $H_2O$ we were not able to trace the complete argon plume. This, however, has no effect on the derived $H_2O$ photodepletion.

The difference between the (un)coated experiments in the depletion rate is linked to the total photodesorption efficiency of the ice. Figure 5.4 shows the comparison of the (un)coated results. The difference between them was fitted with a linear function with the slope of the fit corresponding to the photodesorption rate of (1.0 $\pm$ 0.2) $\times$ $10^{-3}$ molecule $photon^{-1}$. This value represents the total photodesorption efficiency of porous amorphous $H_2O$ ice at 20 K.

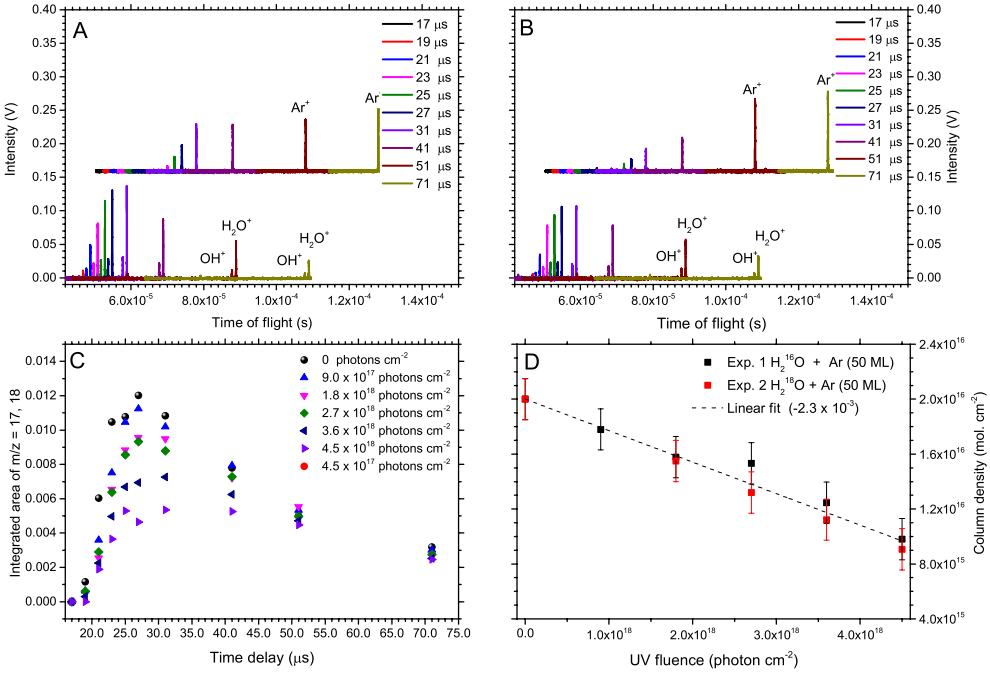


**Figure 5.3:** *Panel A:*LDPI TOF MS spectra of porous amorphous $H_2{}^{16}O$ ice (20 ML) coated with an argon layer (50 ML) collected at 20 K, prior to UV photolysis. For clarity of the figure, the plume profile of $Ar^+$ is separated and vertically offset. *Panel B:* LDPI TOF MS spectra of porous amorphous $H_2O$ + Ar ice after an UV irradiation with a fluence of $3.6 \times 10^{18}$ photons $cm^{-2}$. *Panel C:* Integrated plume profiles of LDPI TOF MS for different UV photon fluence increments. *Panel D:* Photodepletion of the $H_2O$ column density as a function of UV fluence from repeated experiments with $H_2{}^{16}O$ and $H_2{}^{18}O$. Error bars represent the uncertainty on the ice thickness of ±1.5 ML.

## 5.4 Discussion

### 5.4.1 Types of photodesorption

The derived photodesorption rate of amorphous water ice at 20 K is made up of between contributions from intact desorption (as $H_2O$), dissociative desorption (H, OH, or O), and reactive desorption ($H_2$, $O_2$). We are only able to measure the total photodesorption efficiency, but can provide upper limits for the individual contributions. These values are compared with the outcome of previous studies and an overview of all ASW photodesorption rates, reported in the literature, are summarized in Table 1. It should be noted, that not all experimental settings (temperature, ice thickness, UV SED, level of porosity/compactness) in these studies are fully identical, and one-to-one comparisons, for this reason, should be performed with care.

Intact desorption efficiencies measured experimentally for UV photon energies between 7 – 10.2 eV, at 8 - 20 K, are in the range of $(0.55 - 1.3) \times 10^{-3}$ molecule $photon^{-1}$ (Öberg et al. 2009d; Cruz-Diaz et al. 2018; Fillion et al. 2021). Molecular dynamics studies, which consider photon absorption only into the first excited

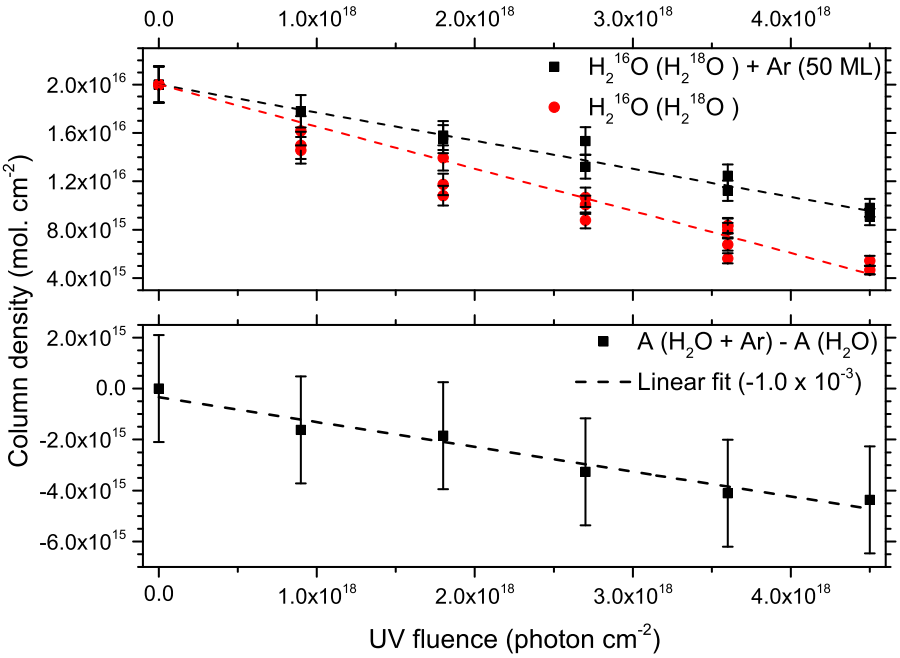


**Figure 5.4:** *Top panel:* $H_2O$ abundance during the UV photolysis of $H_2O$ with and without the argon coating at 20 K. Error bars represent the uncertainty on the ice thickness of ±1.5 ML. *Bottom panel:* The difference in the $H_2O$ abundance between the $H_2O$ and $H_2O$ + Ar experiments resulting in a $H_2O$ photodesorption rate. Error bars represent the propagated uncertainty on the ice thickness, with a final value equal to ± 2.1 ML. Data is fitted with a linear function ($R^2$ = 0.94).

state of water (8.2 – 9.5 eV), yield lower values between (0.14 – 0.5) × $10^{-3}$ molecule photon$^{-1}$ (Kobayashi 1983; Andersson & van Dishoeck 2008; Arasa et al. 2010; Crouse et al. 2015). Based on these theoretical investigations, several mechanisms have been proposed that lead to the intact photodesorption of $H_2O$. An exothermic surface recombination of photodissociation products, OH and H, can result in the $H_2O$ molecule leaving the ice surface. Alternatively, in a 'kick-out' mechanism, an H atom transfers its kinetic energy (following dissociation) to a surface molecule, resulting in the ejection of the latter. DeSimone et al. (2013) suggests a third mechanism, in which excitons generated in the ice upon absorption of UV photons, are near the surface where the charge redistribution of the surface water molecules results in a repulsive electrostatic force, followed by a desorption of a $H_2O$ molecule (Nishi et al. 1984). A so-called DIET (Desorption Induced by Electronic Transition) mechanism, which was experimentally demonstrated to explain the wavelength dependent photodesorption of CO and $N_2$, in pure and CO:$N_2$ mixed ices (Fayolle et al. 2011; Bertin et al. 2013), is not expected to be relevant here, as the favourable process following a UV photon absorption by $H_2O$ molecule is photodissociation (Andersson et al. 2006).

The contribution of dissociative desorption (OH) varies across different studies. Öberg et al. (2009d) derive a value for the OH desorption as roughly equal to the

**Table 5.1:** Summary of water ice photodesorption rate studies, both experimental (Exp) and theoretical (Theor), compared with our work. All desorption rates are given in $\times 10^{-3}$ mol. photon$^{-1}$. The derived rate upper limits are marked by the "<" notation in front of the value. The "total" column represents the loss of water via all photodesorption channels: intact, dissociative and reactive (desorption of $O_2$ requires two water molecules)

| Reference | Exp / Theor | $H_2O$ | OH | $O_2$ | Total | Temp.(K) | Energy (eV) |
|---|---|---|---|---|---|---|---|
| This work | Exp | <1.0 | <1.0 | <0.5 | 1.0 ± 0.2 | 20 | 7 – 10.2 |
| Westley et al. 1995 | Exp | <3.5 | - | - | 3.5 ± 1.8 | 35 | 10.2 |
| Öberg et al. 2009 | Exp | 0.7 ± 0.4 | 0.9 ± 0.5 | - | 1.6 ± 0.9 | 10 | 7 – 10.2 |
| Cruz-Díaz et al. 2018 | Exp | 1.3 ± 0.2 | 0.7 ± 0.3 | 0.6 ± 0.1 | 3.2 ± 0.5 | 8 | 7 – 10.2 |
| Fillion et al. 2021 | Exp | 0.55 ± 0.09 | <0.1 | 0.3 ± 0.2 | 1.25 ± 0.25 | 15 | 7 – 10.2 |
| Andersson, van Dischoeck 2008 | Theor | 0.14 | 0.25 | - | 0.39 | 10 | 8.5 |
| Arasa et al. 2010 | Theor | 0.15 | 0.3 | - | 0.55 | 10 | 8.5 |
| Crouse et al. 2015 | Theor | 0.3 ± 0.2 | 0.3 ± 0.2 | - | 0.6 ± 0.3 | 11 | 8.5 |

efficiency of intact water desorption at low temperatures ($0.9 \times 10^{-3}$ photon$^{-1}$). Cruz-Diaz et al. (2018) provide a yield of $0.7 \times 10^{-3}$ per incident photon at 8 K, lower than their intact photodesorption by a factor of two. In a study by Fillion et al. (2021), OH desorption at 20 K was found to be below their detection limit ($\sim 10^{-4}$ mol. photon$^{-1}$). It is important to note that with the applied experimental methods (IR and QMS), it is difficult to quantify the contribution of OH from photolysis. In the ice, the OH signature overlaps with a vibrational band of $H_2O$ while in the gas phase, the corresponding mass peak (m/z = 17) can be created as a byproduct of electron impact ionization, rather than UV photolysis. The theoretical studies (Arasa et al. 2010; Crouse et al. 2015) result in rates higher than intact desorption, with the ratios of desorbing OH/$H_2O$ between 1 – 2. The absolute calculated desorption yield of OH is lower than the experimental values, by a factor of 2 – 3 ($3 \times 10^{-4}$ photon$^{-1}$).

Reactive photodesorption from water ice is a mechanism previously detected for photoproducts of $H_2$ and $O_2$. The $O_2$ reactive photodesorption rate has been first reported by Öberg et al. (2009d) at a high temperature (100 K), and first quantified by Cruz-Diaz et al. (2018), who determined the reactive photodesorption rate of $O_2$ at 8 K of $(0.6 \pm 0.3) \times 10^{-3}$ per incident photon. In the study by Fillion et al. (2021), the reactive photodesorption rate of $O_2$ at 15 K, was found to be $(0.3 \pm 0.2) \times 10^{-3}$ per incident photon. It is noted that the reactive desorption of other photoproducts, such as $HO_2$ and $H_2O_2$, is yet to be detected. While these are not expected to be major desorption channels, we provide a generous upper limit for both species, equal to 5.0 $\times 10^{-4}$ per incident photon. Theoretical studies were not able to trace $O_2$ (or other species) formation/desorption, due to the short timescales of the modelled processes.

To sum up, the literature provides a range of values for total UV photodesorption of water, between $(0.37 - 3.5) \times 10^{-3}$ per incident photon. These values span an order of magnitude and there is a systematic difference between theoretical and experimental studies. The results of the most recent experimental studies, including this work, agree within a factor of three of each other. This level of agreement is quite acceptable, given the involved uncertainties and differences in ice temperature, used UV photon sources and probing techniques. Photodesorption is a wavelength-dependent process (e.g., Fayolle et al. 2011), hence, the different spectral energy distributions of the applied UV sources can be a reason for differences in measured photodesorption rates. The temperature of the ice during the deposition and irradiation is another parameter that impacts the efficiency of photodesorption. A relative increase in the total photodesorption rate for ices irradiated at temperatures between 8 – 30 K was experimentally measured and found to yield values differing by 15 % (Cruz-Diaz et al. 2018) up to 40 % (Öberg et al. 2009d). A theoretical study by Arasa et al. (2010) is in agreement with these measurements, deriving a relative increase in the total photodesorption rate between 10 – 30 K to be 15%. Furthermore, it should be noted that all derived photodesorption rates come with relatively high uncertainties. In case of experiments it is a combination of errors related to ice column density, UV photon flux, (IR) band strength, or varying pumping efficiencies for different species, adding up to a large error margin on the final photodesorption rates that can be as high as 50 %. In theoretical calculations, a difference of a factor of a few can be due to the use of gas-phase potential energy surface for modelling the interactions between $H_2O$ molecules, using a short time scale, and only exciting the water molecules in the first excited state (Arasa et al. 2010).

The value derived here puts the most accurate upper limit on an experimentally

derived total photodesorption rate of ASW, and it is well within the uncertainty of other experimental studies and a factor of 2 above theoretical results. It provides a basis to constrain each type of photodesorption, intact, dissociative and reactive, with an upper limit for the first two types equal to the total derived photodesorption rate, $1.0 \times 10^{-3}$ molecule photon$^{-1}$. For the reactive desorption, the upper limit is at 0.5 $\times 10^{-3}$ molecule photon$^{-1}$, as for each desorbed $O_2$, a loss of two $H_2O$ molecules is required. These upper limits are based on the assumption that the total photodesorption is dominated by a contribution from only one channel, while the others are set to zero.

### 5.4.2 Photoconversion of $H_2O$ ice

Figure 5.4 allows to distinguish between the effects of photodesorption and photoconversion, during the UV photolysis of $H_2O$ ice. It is worth noting that in the coated experiments, where the depletion due to photodesorption is excluded, after the final UV fluence dose, the remaining column density of $H_2O$ is only about 50% of the initial value. Clearly, upon extended UV irradiation the ice is subject to more processing than photodesorption only.

The photoconversion is a dominant loss channel, depleting the $H_2O$ molecules at a rate of $(2.3 \pm 0.3) \times 10^{-3}$ per UV photon. The depletion of the parent species is expected to result in the formation of photoproducts, $H_2$, OH, $O_2$, $HO_2$, and $H_2O_2$. Considering that water is a dominant species in the interstellar ices, it is somewhat surprising that there is very limited literature on the photoproduct formation yields upon UV photolysis of $H_2O$ ice. Only recently, a first quantitative study of the formation of typically elusive $O_2$ and $H_2O_2$, was reported, also applying LDPI TOF MS (Bulak et al., in press). In experiments favoring bulk processes, a $H_2O$ ice (100 ML thickness) deposited at 20 K was exposed to a UV photon fluence of $1.8 \times 10^{18}$ photons cm$^{-2}$. The formation of both $O_2$ and $H_2O_2$ reaches a balance with available destruction pathways after a UV fluence between $(4.5 - 9.0) \times 10^{17}$ photons cm$^{-2}$, at roughly equal abundances of 1% ($\sim$1 ML) with respect to $H_2O$. Both $O_2$ and $H_2O_2$, require two oxygen atoms to be formed (i.e., two $H_2O$ molecules). As these were the only detected products, the corresponding depletion of the parent species should be 4%. If we assume the same efficiency of photoproduct formation in the experiments with argon coating presented here, exposed to the same irradiation dose, the consumption of water due to photoconversion should be 0.8 ML. This allows us to account for the loss of $H_2O$ via photoconversion into $O_2$ and $H_2O_2$, at least at the early, and from an astronomical point of view, most relevant photolysis stages.

At higher photon fluence, the depletion of $H_2O$ continues at a linear rate, while the abundances of detected photoproducts are expected to remain on the same level or decrease (Bulak et al., in press). This means that the formation of $O_2$ and $H_2O_2$ cannot account for the continuing loss of $H_2O$. In the absence of other detected products, it is not fully clear what exactly happens. Considering the total UV photon fluence in our experiments and the absorption cross section of water ice (Cruz-Diaz et al. 2014b), we estimate a ratio of water molecules in the ice to the number of absorbed photons of $\sim$20. A part of this lost oxygen budget can be locked in the OH and $HO_2$ radicals trapped in the ice. Indeed, H atoms and produced $H_2$ molecules are mobile and can diffuse into the Ar cap, leaving the OH and $HO_2$ radicals in the bulk of the $H_2O$ ice. Nevertheless, this can only account for the limited fraction of the lost budget. Another

possibility is the diffusion of $H_2O$ molecules into the spots ablated by the previous laser pulses. This is due to considerably longer irradiation time (5 hours) than during our previous experiments, resulting in a higher amount of heat dissipated in the ice. This will be addressed in the future studies. This unaccounted loss of $H_2O$ does not affect the low UV fluence data and can only further reduce our reported photodesorption and photoconversion rates, keeping them as strong upper limits.

## 5.5 Astrophysical implications

The values used in the past in gas-grain models for the photodesorption rate of ASW are very close to the value derived here, and that has been measured in a fully independent way. Our value offers a somewhat more strict upper limit and this could be taken into account for future work. A detailed astrochemical model of molecular clouds by Hollenbach et al. (2009), shows that photodissociation and photodesorption are the dominant physical processes impacting the gas-phase abundances from the edges until intermediate depths into the cloud. In their model, at the onset of water ice freeze-out, the water vapour abundance is in 98% due to photodesorption of $H_2O$ which has been formed on grains, with the remainder (of the gas-phase abundance) formed through low temperature gas-phase chemistry. Deeper into the cloud, the percentage drops to 70%, and at intermediate depths into the cloud, goes up again to 92%. In this model, the intact ($H_2O$) and dissociative (OH from $H_2O$ ice) photodesorption rates are set to $1 \times 10^{-3}$, and $2 \times 10^{-3}$ per incident UV photon, respectively. The photodesorption of $O_2$ was considered only from pure $O_2$ ices at $1 \times 10^{-3}$ mol. photon$^{-1}$. These rates were used to reproduce the gas-phase $H_2O$ and (when applicable) $O_2$ abundances towards molecular cloud B68, a star forming cloud in Orion, NGC 2024, and $\rho$ Ophiuchus (Hollenbach et al. 2009; Larsson et al. 2007). In a less-detailed model by Schmalzl et al. (2014), the same intact photodesorption rate, combined with photodissociation and freeze-out rates, successfully matches the abundances of water vapour towards the cold regions of pre- and protostellar cores. Also in this study, the reactive photodesorption (of $O_2$) was not taken into account.

These models use previous laboratory values for intact photodesorption that are largely in line with our work. However, the values for dissociative desorption rate (OH), seem to be consistently lower (see Table 1) than adapted in models. We recommend that these values are updated, as the OH radical, released from the grains via a non-thermal mechanism, contributes to the formation of simple molecules such as CO, $CO_2$, NO, $H_2O$, as well as complex organic molecules, such as $HCOOCH_3$ (Charnley et al. 2001; Vasyunin & Herbst 2013; Shannon et al. 2013; Vasyunin et al. 2017). In addition, based on the work presented here, we propose for future work that the reactive photodesorption rate of $O_2$ is added to the astrochemical models.

In our experiments the photoconversion depletes the $H_2O$ column density twice as fast as the photodesorption. Formation of photoproducts, $O_2$ and $H_2O_2$ can account for the initial photoconversion of water, until a UV fluence of $9.0 \times 10^{17}$ photon cm$^{-2}$, each at a formation level of 1% of $H_2O$ (Bulak et al., in press). At higher photon fluence, the continuing formation of OH radicals can be of significance for further ice chemistry, opening pathways towards oxygen-carrying molecules, such as $CO_2$, $CH_3OH$, HCOOH, or $HCOOCH_3$ (Öberg et al. 2009c, 2010b; Garrod et al. 2008).

It is important to note, that while water is the dominant component of interstellar

ices, other species, including $CO_2$, $CH_4$, $NH_3$, $CH_3OH$ are present and expected to impact the photoconversion as well as photodesorption rates derived for pure water ice. The inclusion of less abundant constituents of interstellar ices in water ice, strongly affects the observed photoconversion. These effects are outlined by Öberg et al. (2010b), where it is demonstrated that the recombination reactions of water are inhibited by up to an order of magnitude due to competitive reactions with other radicals in the ice. In a recent study of photolysis of mixed ices of $H_2O$:$CO_2$, an increasing amount of $CO_2$ in the initial composition, resulted in a more efficient photodepletion of water, a shift in the photoproduct yields to carbon bearing species, and a corresponding decrease in the absolute formation yield of $O_2$ and $H_2O_2$ (Bulak et al., in press). It is also expected that the photodesorption rates of species in mixed ices will differ from its pure equivalents. This will be the topic of future work; the method presented here has the potential to also derive photodesorption rates for different species in mixed ices.

## 5.6 Conclusions

A quantification of photodesorption rates and separating this process from the photoconversion of ASW, is crucial as it allows to balance water abundances between ice and gas in astronomical environments such as dense molecular clouds.

Here we apply an alternative, independent measuring technique of LDPI TOF MS to separate the effect of photodesorption from photoconversion during the UV photolysis of porous amourphous water ice at 20 K. We derive the total photodesorption rate to be $(1.0 \pm 0.2) \times 10^{-3}$ per incident UV photon. This is an average value for the photon energy range equivalent to the secondary UV field in the ISM (7 – 10.2 eV). Based on this value, we place an upper limit on the relative contribution of three channels. Both, the intact ($H_2O$) and dissociative (OH) desorption rates, have an upper limit equal to $1.0 \times 10^{-3}$ per incident UV photon, while for reactive desorption ($O_2$), the limit is equal to $0.5 \times 10^{-3}$ per incident UV photon. It should be noted, that these values apply for pure water ice. Even though water is the dominant species in interstellar ices, also other species will be present that can affect these values. For this also photodesorption rates of mixed ices will be needed and with the new technique presented here, this will be possible.